Photoacoustic tomographic image reconstruction

Internship Report

Trung Thai DO

Master 1 Student in Applied Mathematics, INSA Toulouse

Supervisors : Paul ESCANDE
PhD Applied Maths, CNRS researcher in Toulouse

Contents

1 Introduction

1.1 Laboratory presentation

The Toulouse Institute of Mathematics (IMT, Unité Mixte de Recherche 5219) brings together 240 teacher-researchers and permanent researchers, engineers, technicians and administrative staff as well as 120 doctoral students and around 30 post-doctoral students on average. The laboratory depends on six supervisory authorities: CNRS, INSA, INUC, Toulouse 1 Capitole University, Toulouse-Jean Jaurès University, Toulouse 3 - Paul Sabatier University.

The research themes cover all mathematical fields from the most theoretical aspects to the most applied and are organized around 6 teams which correspond to mathematical sub-disciplines. IMT develops numerous interactions with other sciences and with the socio-economic world, often across teams.

1.2 Context and objective of this internship

Photoacoustic Tomography (PAT) has emerged as a transformative imaging modality with profound implications for biomedical and clinical research. This innovative technique harnesses the principles of multispectral imaging, combining laser-induced optical excitation with ultrasound detection to produce high-resolution images of optical absorption within biological tissues. PAT has unlocked a wealth of opportunities in the fields of medical diagnostics, pre-clinical research, and tissue characterization. It has enabled researchers to delve into the microcosm of biological tissues, uncovering critical insights into their structural and functional properties. Figure 1 illustrates the principle of PAT [1].

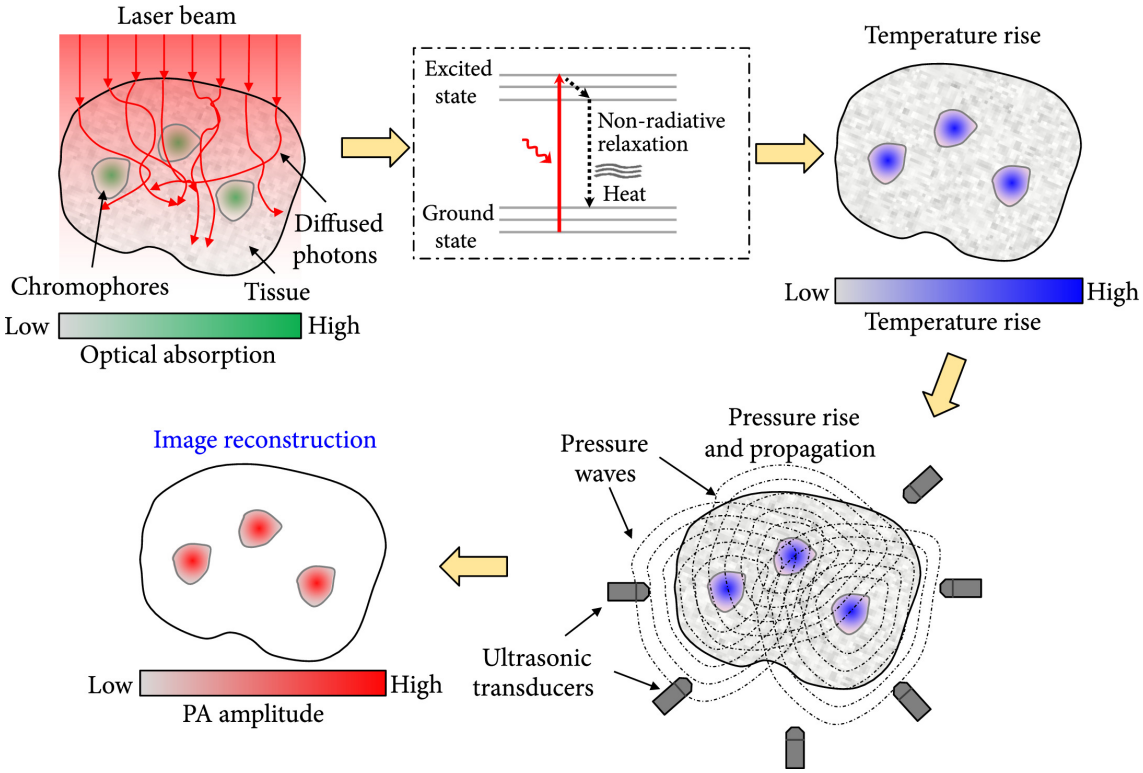

Figure 1: The priciple of PAT

Photoacoustic Tomography (PAT) holds immense promise in the fields of biological and clinical research, offering a unique perspective on imaging the optical absorption characteristics of deep tissue. However, the reconstruction of PAT images is a formidable challenge due to its inherently complex nature. In this paper, we explore innovative strategies for enhancing the reconstruction of PAT images, integrating a spectrum of methods and regularization techniques, including "Least Squares," "Forward-Backward," and "BFGS," alongside both L1 and L2 regularization, within the Plug-and-Play framework. Furthermore, we introduce the Fast and Flexible Deep denoiser Network (FFDnet) as a critical component of our approach.

PAT's reconstruction process necessitates a thorough understanding of the physical modeling, encompassing wave propagation within the tissue and the initial pressure distribution caused by optical absorption. This modeling translates into a linear inverse problem, represented by the equation $g = Ap_0$, where g corresponds to the observed signals, A denotes the measurement operator, and p_0 signifies the initial pressure distribution to be reconstructed. The figure 2 show the observed (measured) signal and the vessal image.

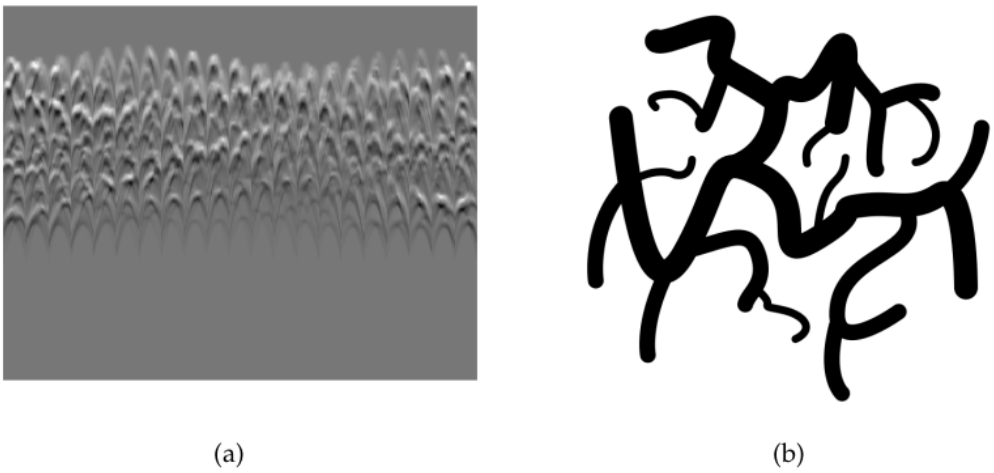

Figure 2: (a) Image of measured signals (time vs detector position) and (b) the corresponding numerical vessel phantom.

While the field of PAT is brimming with potential, one significant challenge lies in the limited availability of comprehensive open-source datasets for research and development. Existing datasets serve as valuable resources for benchmarking and validating reconstruction strategies. However, as the field evolves and diversifies, the scarcity of diverse and realistic open-source data becomes increasingly apparent.

To address this limitation, we underscore the critical importance of creating synthetic datasets tailored to the needs of PAT researchers. These synthetic datasets are designed to simulate numerical vessel phantoms . By generating such synthetic data, we aim to bridge the gap between the limited availability of real-world data and the burgeoning demands of PAT research and development, ultimately advancing the capabilities of PAT imaging.

2 Mathematical modeling

2.1 Physical modeling

Wave Propagation in Tissue: PAT begins with the fundamental process of wave propagation within biological tissues. When light is absorbed by endogenous chromophores (e.g., hemoglobin and melanin) or exogenous contrast agents, it induces a localized temperature rise. This thermal expansion results in the generation of an acoustic pressure wave. The primary objective of PAT is to map the initial pressure field, denoted as p_0, created by the optical absorption event, to the entire pressure field p across spatial coordinates (R^3) and time ($[0, T]$). The linear operator F plays a pivotal role in this mapping process, representing the wave equation – a second-order linear partial differential equation (PDE). This PDE governs the behavior of the acoustic wave as it propagates through the tissue.

Numerical Discretization: To work with PAT data computationally, the continuous wave propagation must be discretized. The resulting matrix operator F is of substantial size, typically $(N^3 \times n_T) \times N^3$, where N^3 represents the grid size discretizing the tissue domain, and n_T is the number of time samples. It is crucial to acknowledge that this matrix can be enormous, making practical storage and computation challenging.

2.2 Measurement

In the context of Photoacoustic Tomography (PAT), the pressure generated by the optical absorption of tissue is a fundamental concept. When light is absorbed by endogenous molecules (such as hemoglobin or melanin) or exogenous contrast agents within biological tissues, it leads to a localized increase in temperature. This temperature increase causes a rapid expansion of the tissue, creating a small pressure increase. This pressure increase results in the generation of an acoustic wave.

The pressure caused by the generated ultrasonic delta wave in a homogeneous acoustic medium is given by: [2]

$$\frac{\partial^2 p(\boldsymbol{r}, t)}{\partial t^2} - c^2 \nabla^2 p(\boldsymbol{r}, t) = \Gamma H(\boldsymbol{r}) \frac{\partial \delta(t)}{\partial t}. \tag{1}$$

At initial condition:

$$p(r, t)|_{t=0} = \Gamma H(\boldsymbol{r}), \quad \left.\frac{\partial p(\boldsymbol{r}, t)}{\partial t}\right|_{t=0} = 0. \tag{2}$$

the pressure given by:

$$p(x, t) = \frac{\delta}{\delta t} \frac{1}{ct} \int_{S(x,t)} H(r) dS(x, t). \tag{3}$$

where S(x,t) is a circle with center x and radius $ct = |r - r'|$.

In PAT, the pressure field p, which encodes valuable information about tissue composition and properties, is not directly measured. Instead, a network of external sensors is employed to detect the acoustic waves generated by the initial pressure p_0. These sensors are associated with 2D surfaces $S_i \subset \mathbb{R}^3$, each responsible for recording the pressure. The measurement operator Mi is responsible for mapping the pressure field p to measurable signals $g_i(t)$, which represent the acoustic wave's temporal evolution at each sensor's location:

$$g_i(t) = \int_{S(x,t)} p(x, t) dS(x, t). \tag{4}$$

The global measurement operator $M = (M_i)_{i=1}^n$, formed as the concatenation of all individual measurements, serves as the bridge between the pressure field and the observed signals, facilitating the collection of data for image reconstruction.

2.3 Linear Inverse Problem

Overall, the physical modeling of PAT leads to a linear inverse problem represented by the equation $g = Ap_0$. Here, g represents the observed signals, which are the outcomes of the measurements. The matrix operator A is formed as $A = MF$, combining the wave propagation operator and the measurement acquisition.

Consider an operator $A : X \to Y$ between two Hilbert spaces, given measured noisy data: $y = Ax + \epsilon$ where ϵ describes the noise in the measurement (usually an additive white Gaussian noise).

A classical approach of model-based methods consists of solving an optimization problem:

$$\hat{x} = \text{argmin} \, \|Ax - y\|_2^2 + \lambda R(x) \tag{5}$$

where R(x) is a regularization term depending on x. Many hand-crafted regularizers are used in the literature, depending on application, such as Tikhonov (square of $L2$-norm), $L1$-norm, total variation ($L1$-norm of the gradient) or Cauchy regularization (using the pdf function of cauchy distribution), etc.

Learning-based methods, on the other hand, rely on the training of models, often built around Convolutional Neural Networks (CNNs). These models are trained through an optimization process that revolves around minimizing a loss function. This training procedure is carried out on a curated dataset that comprises pairs of images: one that has undergone degradation (referred to as the degraded image) and its corresponding clean counterpart.

During this internship, the focus is on training a specific type of CNN model known as FFDNet (Fast and Flexible Denoiser) for the purpose of Photoacoustic Tomography (PAT) image reconstruction. FFDNet is a deep learning model tailored to image denoising tasks and has the potential to be highly effective in improving the quality of PAT image reconstructions.

3 Dataset creation

One of the challenges in the field of Photoacoustic Tomography (PAT) is the availability of comprehensive open-source datasets for research and development. To address this limitation, we created a synthetic dataset to simulate numerical vessel phantoms. This dataset serves as a valuable resource for testing and validating image reconstruction algorithms in PAT. In this section, we describe the methodology used to generate this synthetic dataset, which includes the creation of vessel phantoms with varying characteristics. Figure 3 is an example of a numerical vessel phantom.

3.1 Phantom design

- Vessel Generation: The first step in dataset creation involved generating vessel phantoms. We used Bézier curves to define the shape of vessels in a 2D space. Bezier curves are versatile tools for designing complex shapes, making them suitable for emulating vessel geometries. We created various vessel structures by defining Bezier curves and adjusting control points to shape vessels of different sizes and configurations.

- Vessel Thickness: To introduce diversity in vessel characteristics, we specified the thickness of vessels. Vessel thickness was controlled to simulate the varying anatomical structures that may

Figure 3: Example of a vessel phantom

be encountered in real biological tissues, offering a realistic representation of vessels with varying diameters.

- Spline Discretization: Bézier curves were discretized using linear interpolation to create discrete points along the vessel path. This step ensured that the vessel's shape and trajectory were represented as a set of connected points, which were subsequently used for simulation.

- Circle Insertion: To simulate the presence of vessels within tissue, we inserted circular cross-sections along the interpolated vessel paths. The size and location of these circular structures were varied to represent different vessel cross-sections.

Bezier curves:

The idea of this method [1] consists in using cubic Bezier curves to interpolate points randomly chosen with criteria inside a unit square such that the resulting curve is not too rough.

First, we generate N points within a 2D plane unit square in a way that the minimum distance between each point should be c/N with $c > 0$. To do that, we generate N random points inside a loop, if the result satisfy the condition on the minimum distance, we get out of the loop. If after all loops, the minimum distance is not satisfied, then we take the points randomly generated at the final loop. The coordinates of points are then multiplied with a scaling factor s that we choose in order to better represent a stain shape. Next, the random points chosen are sorted in counter clockwise order. We denote the sequence of points sorted respectively $P_0, P_1, \ldots, P_{N-1}$. We then append P_0 to the tail of the sequence to have a close cycle of points, $P_0, P_1, \ldots, P_{N-1}, P_0$. These points will be interpolated and will all lie on the resulting curve. The intermediate control points

[1] https://stackoverflow.com/a/50751932

for each couple of consecutive points in the sequence are defined by two parameters *rad* and *angle*.

Take an example of P_0 as the start point and P_1 as the end point, the Bezier curve interpolating P_0 and P_1 will have intermediate control points called $Q_{0,1}$ and $Q_{1,0}$, where $Q_{0,1}$ and $Q_{1,0}$ lie on the circle with center P_0 and P_1 respectively and with a radius to be fixed. The position of $Q_{0,1}$ and $Q_{1,0}$ on the circle are fixed with another parameter $angle_{0,1}$ and $angle_{1,0}$, which describe the angle in radians between the horizontal line passing through P_0 toward -inf and the ray passing through P_0 toward $Q_{0,1}$ (and respectively the angle in radians between the horizontal line passing through $Q_{1,0}$ toward $-\infty$ and the ray passing through $Q_{1,0}$ toward P_1). The angles are calculated as the mean between the direction of adjacent points, in order to have a smooth curve. The parameter *rad* is chosen to be varied from 0 to 1, proportioned to the distance between adjacent points. The larger *rad* is, the sharper the curve segment linking points is (except for extremely small rad). This behavior is illustrated in Figure 4.

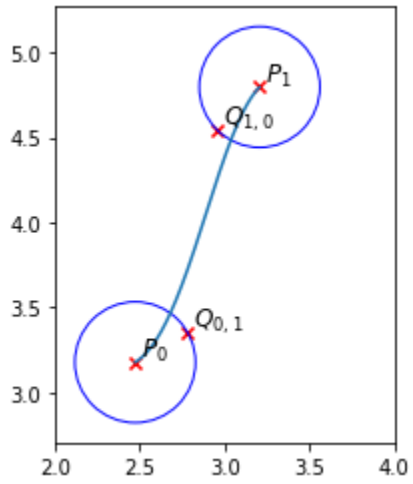

Figure 4: Cubic Bezier curves with 4 control points, the two intermediate points are calculated with a fixed radius, $angle_{0,1} = \frac{\pi}{6}$ and $angle_{1,0} = \frac{\pi}{4}$

After computing all intermediate control points, we can construct cubic Bezier curves to interpolate $P_0, P_1, \ldots P_{N-1}, P_N$ with the explicit expression:

$$\begin{aligned}\mathbf{B}(t) &= \sum_{i=0}^{n} \binom{n}{i} (1-t)^{n-i} t^i \mathbf{P}_i \\ &= (1-t)^n \mathbf{P}_0 + \binom{n}{1} (1-t)^{n-1} t \mathbf{P}_1 \\ &+ \cdots + \binom{n}{n-1} (1-t) t^{n-1} \mathbf{P}_{n-1} + t^n \mathbf{P}_n, \quad 0 \le t \le 1\end{aligned}$$

where $\binom{n}{i}$ are the binomial coefficients.

3.2 Rasterization and Signal Simulation

- Rasterization: The generated vessel phantoms were rasterized into 2D images. Each image represented a cross-section of the simulated tissue with vessels. The resolution of the images was chosen to match typical PAT imaging parameters.

- Acoustic Signal Simulation: To create the acoustic signals, we utilized the principles of PAT. The initial pressure fields associated with each vessel cross-section were simulated based on the absorbed optical energy within the vessels. Theoretical models and known tissue properties were used to simulate the generation and propagation of acoustic waves.

3.3 Dataset Characteristics

The resulting dataset comprises a diverse range of numerical vessel phantoms, each defined by distinct vessel geometries, thicknesses, and orientations. This dataset is instrumental in assessing and fine-tuning image processing techniques, including denoising, reconstruction, and other image enhancement methods in the context of PAT.

3.4 Benefits of the Custom Dataset

The advantage of creating a custom dataset is the ability to tailor it to specific research needs. Our dataset provides researchers with a valuable resource for evaluating and benchmarking image processing algorithms in the challenging domain of PAT. Furthermore, it bridges the gap caused by the lack of readily available open-source datasets for numerical vessel phantoms, facilitating progress in this field.

This custom dataset serves as a cornerstone for our research and will enable us to rigorously evaluate the performance of image processing methods, including our application of the FFDnet model for image denoising. By leveraging this dataset, we aim to contribute to the advancement of image processing techniques in Photoacoustic Tomography, ultimately enhancing the quality and accuracy of image reconstructions for biomedical applications.

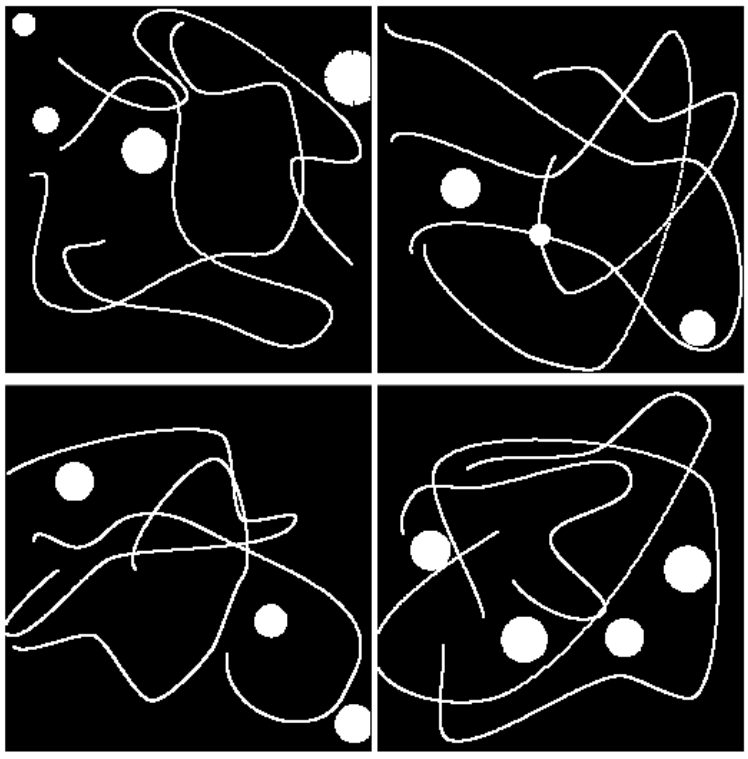

Figure 5: Example of simulated vessels

The figure 5 gives some examples of simulated vessel that we have made using the above method.

4 Methodology

In the realm of Photoacoustic Tomography (PAT) for image processing, the process of image reconstruction stands as a pivotal juncture where raw data is transformed into interpretable and informative images. The choice of the reconstruction method significantly influences the quality, accuracy, and robustness of the images generated through PAT. This section is dedicated to a comprehensive exploration of diverse reconstruction techniques that have been applied and fine-tuned to address the complex challenges unique to PAT.

Our objective is to shed light on the principles, nuances, and potential advantages of each reconstruction method, providing a detailed understanding of their roles in enhancing PAT image processing. These methods encompass a broad spectrum of techniques, from traditional least square approaches to more advanced and cutting-edge optimization algorithms with various regularization strategies.

We have meticulously evaluated these reconstruction methods, considering their performance in terms of image quality, noise reduction, and computational efficiency. To quantitatively assess their effectiveness, we employ a standardized evaluation metric, the Signal-to-Noise Ratio (SNR), which allows us to compare and contrast the quality of reconstructed images. As we embark on this journey through the reconstruction methods, we aim to showcase the diverse strategies that researchers have at their disposal to overcome the challenges of PAT image reconstruction and ultimately contribute to the advancement of this transformative imaging modality.

4.1 Signal-to-Noise Ratio (SRN)

To measure the error of approximations, we will use the Signal-to-Noise Ratio (SNR), which is the negative log-scale of the relative error, defined by:

$$\mathrm{SNR}(h, \hat{h}) = -10 \log_{10} \left(\frac{\|h - \hat{h}\|_2^2}{\|h\|_2^2} \right) \text{ in decibel (dB)} \tag{6}$$

where $h \in \mathbb{K}^N$ is the true signal and $\widehat{h} \in \mathbb{K}^N$ is the reconstructed signal (or approximated signal). The principle is simple, the higher SNR, the better approximation.

4.2 Least Square

The Least Squares method serves as the foundational approach for image reconstruction in PAT. Its primary objective is to mitigate the disparities between the observed PAT signals and those forecasted by our numerical vessel phantoms. Essentially, this entails resolving a linear inverse problem with the aim of identifying an image that best aligns with the recorded data. Least Squares optimization strives to discover an image that minimizes the sum of squared variances between the anticipated and observed signals. This method establishes a robust baseline for the comparative assessment of more sophisticated reconstruction techniques.

We employed the *scipy.sparse.linalg* function from the scipy library. This function is designed to address linear systems of equations or optimization problems. It can be applied to solve equations of the form $Ax = b$ or minimize $||Ax - b||^2$. In our context, A represents the PAT matrix, and b denotes the initial pressure distribution.

4.2.1 Non-Negative Least Square

Non-Negative Least Squares (NNLS) reconstruction presents a logical extension of the Least Squares method, introducing a crucial constraint: the requirement for all pixel values in the reconstructed image to be non-negative. In the realm of Photoacoustic Tomography (PAT), this constraint is of paramount importance to guarantee that reconstructed images correspond to physically meaningful quantities.

In PAT, it is imperative that reconstructed images do not yield negative pixel values, as negative values lack physical interpretation and can lead to erroneous conclusions. By imposing this non-negativity constraint, we enhance the interpretability and physical accuracy of the reconstructed images.

To implement this constraint, we developed a dedicated function designed to solve the optimization problem of minimizing $||Ax - b||^2$ while ensuring that all pixel values in the image, represented by the vector x, remain non-negative ($x \geq 0$). This additional constraint serves to refine the image reconstruction process, resulting in more reliable and physically relevant outcomes. The NNLS reconstruction method is essentially a projected gradient descent approach. It leverages the power of gradient descent to minimize the objective function while consistently projecting the solution onto the non-negative space at each iteration. This combination of gradient descent with the non-negativity constraint ensures that the reconstructed image remains physically valid and enhances the quality of image reconstruction in PAT.

4.2.2 L2 Penalized Least Square

L2 Penalized Least Square reconstruction extends the classic Least Squares method by introducing L2 regularization to the optimization problem. L2 regularization entails the addition of a penalty term to the optimization objective, which serves to discourage the emergence of excessively large pixel values in the reconstructed image. This regularization strategy fulfills various essential roles in the context of image reconstruction.

One primary advantage of L2 regularization is its ability to mitigate the impact of noise in the observed data. By penalizing large pixel values, it promotes the creation of smoother and more stable reconstructed images. This feature is especially valuable when dealing with noisy or incomplete data, as it helps enhance the quality of image reconstruction.

To achieve L2 regularization, you should introduce a term represented as $\frac{\lambda}{2}||p||^2$ into the optimization problem. This term is commonly referred to as the L2 regularization term or the ridge penalty. This term contributes to the overall optimization objective, facilitating the creation of more reliable and noise-resistant reconstructed images.

4.3 Forward-Backward Splitting

Forward-Backward Splitting is an iterative optimization technique commonly used to solve inverse problems in the context of imaging. It offers versatility and can accommodate various regularization schemes.

4.3.1 L1 Regularization

L1-Regularized Image Reconstruction is a specific application of the Forward-Backward Splitting method that incorporates L1 regularization. L1 regularization is particularly valuable in Photoacoustic Tomography (PAT) for feature extraction and noise reduction. Sparse representations are often preferred to emphasize essential features while reducing the impact of noise.

To solve the inverse problem (1) with $R(p) = ||p||_1$, FBS employs the proximal gradient method. The solution can be expressed as:

$$x^* = prox_{tR(x)}(x^* - t(A^*(Ap - s))). \tag{7}$$

In this equation, the proximal operator, denoted as $prox(f)$, is defined as:

$$argmin(f(u) + \frac{1}{2}||u - x||^2)$$

. The proximal operator aims to find the point u that minimizes the given function $f(u)$ while ensuring that the norm of $(u - x)$ is controlled. This operation is a crucial component of the FBS algorithm used to achieve L1-regularized image reconstruction.

4.3.2 Total Variation-L2 Regularization

Incorporating Total Variation (TV) regularization within the framework of Forward-Backward Splitting (FBS) is instrumental in promoting piecewise constant structures within reconstructed images. This regularization method offers significant advantages in scenarios where image features exhibit sharp edges or substantial variations. Total Variation regularization excels at denoising images while simultaneously preserving crucial structural details.

The Total Variation L2 of p is defined as:

$$TV(p) = \|\nabla(p)\|_{TV} = \sum_{i=1}^{N} \|\nabla(p)[i]\|_2 = \sum_{i=1}^{N} \sqrt{\sum_{j=1}^{d} (\delta_j(p)[i])^2}. \tag{8}$$

Total Variation regularization, often referred to as Isotropic Total Variation, is a powerful approach for enhancing image quality. It encourages piecewise constant structures, making it ideal for scenarios with complex or sharp-edged features. By effectively reducing noise while preserving essential image details, this regularization technique plays a pivotal role in improving image reconstruction quality.

4.3.3 Cauchy Regularization

In this section, we will elucidate some crucial properties of scalar Cauchy penalty functions, denoted as $\varphi(\cdot, y)$, that play a pivotal role in the solvability of equation (1). In contrast to other distributions within the same family, the probability density function of the Cauchy distribution, when centered at the origin, offers a unique advantage. It can be explicitly expressed in closed-form, characterized by a positive shape parameter y, where $y > 0$. The expression for this probability density function is as follows [3]:

$$p(t, y) = \frac{1}{\pi} \frac{y}{y^2 + t^2}, t \subset \mathbb{R} \tag{9}$$

The Cauchy penalty function can be precisely defined by considering the negative log-likelihood of the corresponding Cauchy Probability Density Function (PDF). For any value of t belonging to the set of real numbers, this penalty function can be expressed as follows:

$$\phi(t, y) = -log(\frac{y}{y^2 + t^2}) \tag{10}$$

The advantage of using Cauchy regularization in inverse problems lies in its robustness against outliers and its ability to promote sparsity. It effectively reduces the impact of noisy or extreme data points, encourages solutions with fewer non-zero values (sparsity), and offers flexibility in tuning the balance between robustness and sparsity. This makes it a versatile and effective choice for various inverse problem scenarios.

4.4 BFGS algorithm

For resolving unconstrained optimization issues, the well-known quasi-Newton Broyden-Fletcher-Goldfarb-Shanno (BFGS) [4] approach is used.

Let $f : \mathbb{R} \times \mathbb{R}$ be a function that is continuously differentiable. The unrestricted optimization task involves minimizing f(x) with $x \in \mathbb{N}$.

In this instance, the function to be minimized is:

$$f(p) = \frac{1}{2}\|Ap - s\|^2 + R(\nabla p) \tag{11}$$

where R denotes the Cauchy regularization.

The search direction g_k is first calculated as follows: $g_k = B_k^{-1}\nabla f(x_k)$, where B_k is an approximation of the Hessian matrix at x_k.

Additionally, the BFGS formula updates the matrix Bk:

$$B_{k+1} = B_k + \frac{\mathbf{y}_k\mathbf{y}_k^{\mathrm{T}}}{\mathbf{y}_k^{\mathrm{T}}\mathbf{s}_k} - \frac{B_k\mathbf{s}_k\mathbf{s}_k^{\mathrm{T}}B_k^{\mathrm{T}}}{\mathbf{s}_k^{\mathrm{T}}B_k\mathbf{s}_k} \tag{12}$$

such that $y_k = g_{k+1} - g_k$ and $s_k = x_{k+1} - x_k$.

We repeat this process with an acceptable α_k that satisfies Wolfe conditions:

$$x_{k+1} = x_k - \alpha_k \times g_k$$

. BFGS requires $O(n^2)$ memory to store the full Hessian matrix for an n-dimensional problem. This can be computationally expensive and impractical for high-dimensional problems.

Instead of storing the full Hessian matrix, L-BFGS uses a limited-memory approach. It stores a limited number (m) of vectors representing the changes in gradient and the corresponding changes in parameter values over a limited history of iterations.

L-BFGS uses these stored vectors to approximate the Hessian-vector product and compute a search direction, which reduces the memory requirements to $O(m \times n)$, where m is much smaller than n. L-BFGS is particularly well-suited for high-dimensional optimization problems, where storing and computing the full Hessian matrix would be impractical.

5 FFDNet within the Plug-and-Play (PnP) Method

The Plug-and-Play (PnP)([5], [6]) method offers a flexible framework for solving inverse problems by integrating denoisers as components within an iterative optimization process. In our work, we leverage the efficiency and denoising capabilities of the Fast and Flexible Denoising Network (FFDNet) model as a key denoising component within the PnP method.

The FFDNet model ([7], [8]), being a deep learning-based denoiser, is well-suited for capturing complex noise patterns in images. By incorporating FFDNet into the PnP framework, we exploit its ability to learn intricate noise characteristics and enhance the quality of the reconstructed image in each iteration.

The choice of FFDnet for training was driven by its adaptability to complex noise patterns, computational efficiency, and flexibility in learning noise representations.

The initial step of our image denoising and reconstruction framework involves reshaping the input image into four sub-images, each serving as a patch. These patches, along with a corresponding noise level map, are then input to the Fast and Flexible Denoising Network (FFDNet).

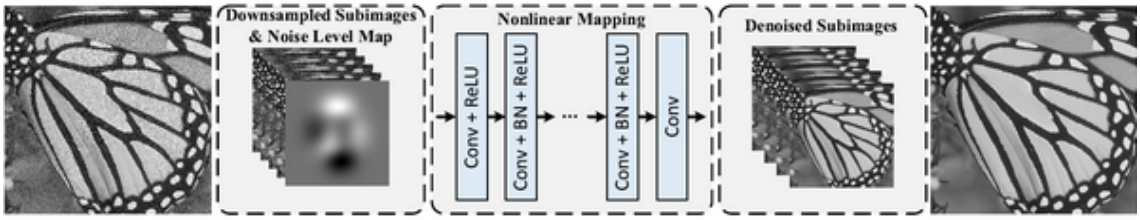

Figure 6: FFDnet Architecture

Principle of FFDNet: FFDNet operates on a patch-by-patch basis and is characterized by the following principles:

- Patch-Based Processing.
- Joint Denoising with Noise Level Map.
- Efficiency and Real-Time Processing.
- Sub-Image Reconstruction.
- Training with Diverse Noise Levels.

Integration into the PnP Method: FFDNet, with its patch-based denoising strategy and adaptability to different noise levels, seamlessly integrates into the iterative PnP method. The denoised sub-images obtained from FFDNet serve as crucial components in the iterative image reconstruction process within the PnP framework.

5.1 Reconstruction Using FISTA and ADMM Algorithms

We use two well-known optimization methods, the Alternating Direction Method of Multipliers (ADMM) and the Fast Iterative Shrinkage-Thresholding Algorithm (FISTA), to further improve our image reconstruction process. In our situation, the optimization issue is always:

$$f(p) = \frac{1}{2}\|Ap - s\|^2 + R(\nabla p) \tag{13}$$

FISTA Algorithm [9]: FISTA is a powerful optimization algorithm known for its convergence speed in solving convex optimization problems. In the context of image reconstruction, FISTA efficiently leverages the sparsity-promoting properties of certain image representations. By integrating FISTA into our framework, we aim to expedite the convergence of our reconstruction process while maintaining the fidelity of the solution.

The FISTA algorithm:

1. Initialize $p_0, y_0, t_0 = 1$.

2. Iterations:

$\cdot\ y_k = p_k + \dfrac{t_{k-1} - 1}{t_k}(p_k - p_{k-1})$

$\cdot\ p_{k+1} = \text{argmin}_p \left(\dfrac{1}{2}\|Ap - s\|^2 + R(\nabla p) + \dfrac{1}{2t_k}\|p - y_k\|_2^2\right)$

$\cdot\ t_{k+1} = \dfrac{1 + \sqrt{1 + 4t_k^2}}{2}$

$\cdot\ k = k + 1$

3. Repeat step 2 until convergence.

ADMM Algorithm [10]: The Alternating Direction Method of Multipliers (ADMM) is a versatile algorithm for solving constrained optimization problems. ADMM is particularly effective when dealing with problems that can be decomposed into smaller, more manageable subproblems. In our reconstruction pipeline, ADMM aids in enforcing constraints and enhancing the stability of the overall optimization process.

Mathematical formulation: $min_{p,z}(\frac{1}{2}\|Ap - s\|^2 + R(\nabla p))$ subject to $\nabla p - z = 0$

The ADMM algorithm:

1. Initialize p^0, z^0, λ^0 (Lagrange multiplier).

2. Iterations:

$\cdot\ p^{k+1} = \text{argmin}_p \left(\frac{1}{2}\|Ap - s\|^2 + \frac{\rho}{2} \left\| \nabla p - z^k + \lambda^k \right\|_2^2 \right)$

$\cdot\ z^{k+1} = \text{argmin}_z \left(R(z) + \frac{\rho}{2} \left\| \nabla p^{k+1} - z + \lambda^k \right\|_2^2 \right)$

$\cdot\ \lambda^{k+1} = \lambda^k + \rho \left(\nabla p^{k+1} - z^{k+1} \right)$

$\cdot\ k = k + 1$

3. Repeat step 2 until convergence.

5.2 Integration and Results

The seamless integration of the FFDNet model within the PnP method, coupled with the refinement offered by the FISTA and ADMM algorithms, results in a comprehensive image reconstruction framework. In the following sections, we present experimental results and comparative analyses to demonstrate the efficacy of our approach in achieving high-quality reconstructed images with reduced noise and enhanced details.

6 Experimental results and analysis

In this section, we present the results obtained from the application of various image reconstruction methods on vessel images corrupted with additional Gaussian noise $\epsilon = \mathcal{N}(0, \sigma^2)$. The Signal-to-Noise Ratio (SNR) is utilized as a metric to evaluate the quality of the reconstructed images.

6.1 Reconstruction Methods and SNR Results

To initiate the reconstruction process, we constructed observations using the matrix of the PAT A and a signal u. The observations were further processed to solve the inverse problem, introducing additional Gaussian noise with σ is randomly $[0.05, 0.1]$. Subsequently, various reconstruction methods were applied, leading to the following SNR results:

The SNR results of various image reconstruction methods provide valuable insights into their effectiveness in restoring vessel images corrupted with additional Gaussian noise. Let's delve into the analysis of the presented results:

Least Squares Method: This method acts as our starting point, providing a decent Signal-to-Noise Ratio (SNR) of 4.76 dB. Although it doesn't explicitly include any special constraints, it sets the stage for comparing more advanced techniques.

Table 1: Summary of Reconstruction Methods and Signal-to-Noise Ratios (SNR)

Method	Iterations	SNR (dB)
Least Squares	-	4.76
Non-Negative Least Squares	100	4.52
L2 Regularized Least Squares	100	2.98
L2-L1 Regularized Least Squares	100	2.98
Total Variation (TV) Regularization	100	4.69
Cauchy Regularization	100	2.98
Cauchy BFGS	100	8.52

Non-Negative Least Squares: By enforcing non-negativity in the reconstruction process, this method achieves a competitive SNR of 4.52 dB. This is especially handy in situations where negative values wouldn't make sense.

L2 Regularized Least Squares: Adding L2 regularization aims to keep the solution's norm in check, preventing overfitting. However, the SNR of 2.98 dB suggests that we might need to fine-tune the strength of regularization.

L2-L1 Regularized Least Squares: This approach combines L2 and L1 regularization, striving for a balance between smoothness and sparsity in the reconstructed image. The SNR result echoes that of L2 regularization, signaling the need for careful adjustment of regularization parameters.

Total Variation (TV) Regularization: Known for maintaining edges and promoting sparsity, TV regularization demonstrates strong performance with an SNR of 4.69 dB. This indicates its effectiveness in dealing with specific noise characteristics found in vessel images.

Cauchy Regularization: Leveraging the robust Cauchy distribution, this method achieves an SNR of 2.98 dB. While it shows resilience to outliers, further exploration is needed to optimize its performance for the given dataset.

Cauchy BFGS: These methods, employing the Broyden-Fletcher-Goldfarb-Shanno (BFGS) optimization algorithm, stand out with an impressive SNR of 8.52 dB. This highlights the effectiveness of iterative optimization techniques in improving reconstruction quality.

In summary, the findings suggest that iterative optimization methods, especially those using the BFGS algorithm, outperform other regularization techniques when reconstructing vessel images from noisy observations. Adjusting the regularization parameters is crucial for the success of these methods and warrants further investigation.

The figure 7 represents the convergence of cost functions for different reconstruction methods, we see also the BFGS is the best model.

The two figure 8 and 9 represents the original image and the reconstructed image.

6.2 Training of FFDnet Model for FISTA and ADMM

In the second phase of our experiments, the Fast and Flexible Denoising Network (FFDnet) was trained to obtain optimal denoising parameters. Utilizing a GPU with 32 GB of RAM, we achieved efficient training with batch sizes of 192, completing 400 iterations in approximately 10 minutes. Notably, it is important to mention that data was created directly during the training phase.

The parameters derived from the FFDnet model were subsequently applied to the FISTA and ADMM algorithms, with coefficent σ of the gaussian noise now being randomly in rang $[0.2, 0.3]$.

We can clearly see in figure 10 that ADMM algorithm is better than FISTA, it is obvious because the SNR ratio of ADMM is better than FISTA (6.49 dB vs 4.70 dB)

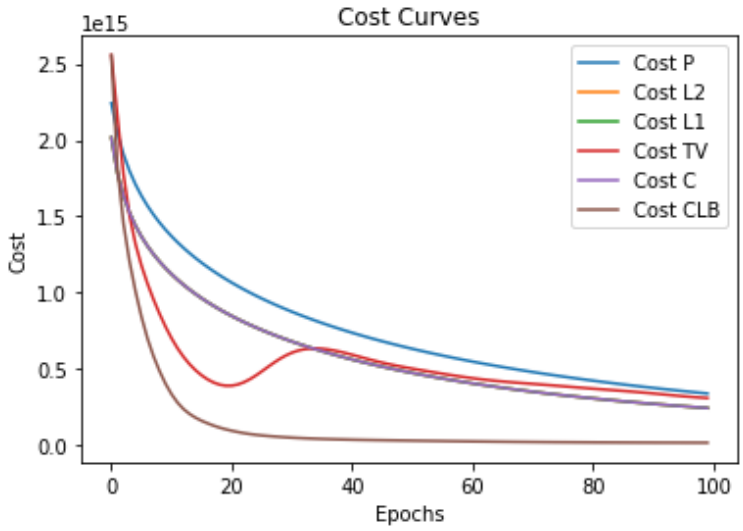

Figure 7: Convergence of cost functions for different reconstruction methods

Figure 8: Original image

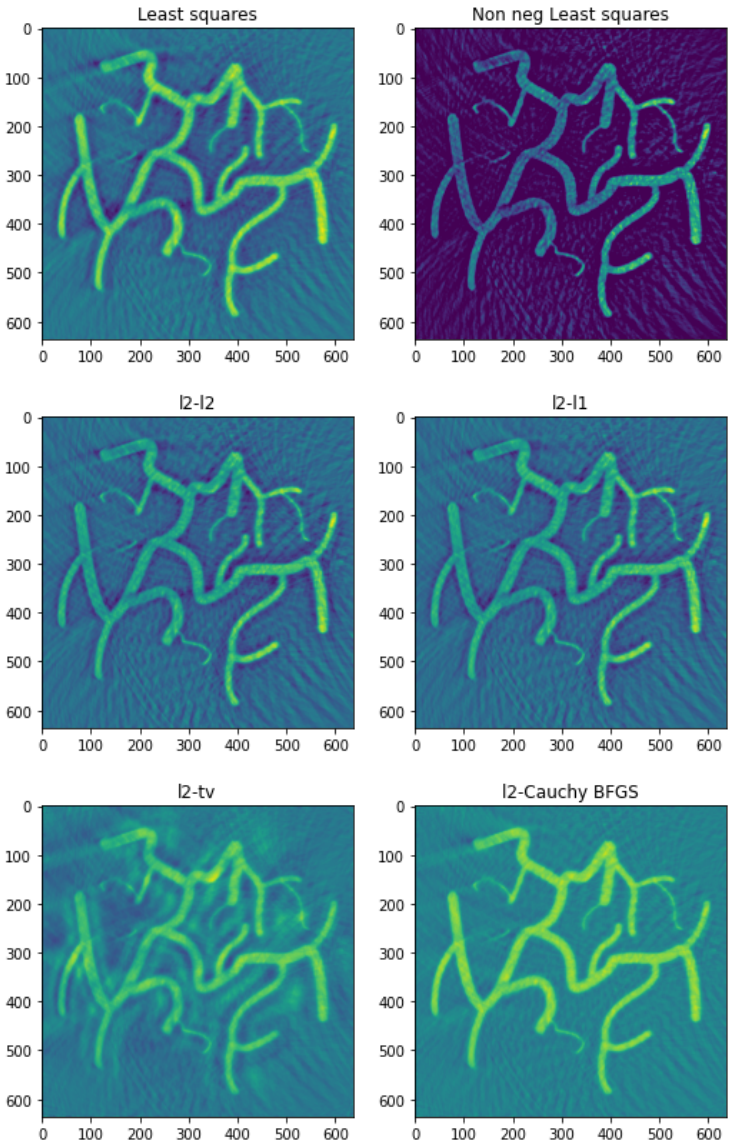

Figure 9: Image reconstruction with different methods

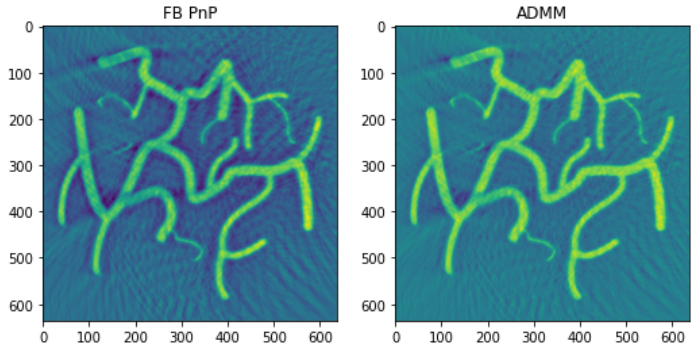

Figure 10: Image reconstruction with FISTA and ADMM

7 Conclution

In conclusion, this report presents a thorough exploration of mathematical modeling, dataset creation, and various reconstruction methodologies to address an inverse problem in Photoacoustic Tomography image reconstruction, an innovative imaging technique that melds laser-induced optical excitation with ultrasound detection to yield high-resolution images of optical absorption in biological tissues. The focus of this exploration lies in leveraging the FFDnet model within the Plug-and-Play framework to tackle the intricate inverse problem encountered in 3D PAT.

The Plug-and-Play methodology, grounded in the principles of computational imaging, introduces a unique strategy to elevate image reconstruction in PAT. By seamlessly integrating the denoising capabilities of FFDnet into the reconstruction process, the objective is to augment image quality and alleviate the impact of approximate sensor geometries on the final results.

Throughout this internship, the theoretical underpinnings, numerical methods, and potential advantages of this pioneering approach are systematically presented. The overarching goal is to contribute a significant step forward in the field of photoacoustic tomography, offering a promising avenue for enhanced image reconstruction and furthering the capabilities of this cutting-edge imaging modality.

References

[1] L. Li and L. V. Wang, "Recent advances in photoacoustic tomography," *BME Frontiers*, vol. 2021, p. 9823268, 2021. [Online]. Available: https://spj.science.org/doi/abs/10.34133/2021/9823268

[2] X. L. Dean-Ben, V. Ntziachristos, and D. Razansky, "Acceleration of optoacoustic model-based reconstruction using angular image discretization," *IEEE Transactions on Medical Imaging*, vol. 31, no. 5, pp. 1154–1162, 2012.

[3] A. Achim, L. Calatroni, S. Morigi, and G. Scrivanti, "Space-variant image reconstruction via cauchy regularisation: Application to optical coherence tomography," *Signal Processing*, vol. 205, p. 108866, 2023. [Online]. Available: https://www.sciencedirect.com/science/article/pii/S0165168422004054

[4] D.-H. Li and M. Fukushima, "On the global convergence of the bfgs method for nonconvex unconstrained optimization problems," *SIAM Journal on Optimization*, vol. 11, no. 4, pp. 1054–1064, 2001. [Online]. Available: https://doi.org/10.1137/S1052623499354242

[5] U. S. Kamilov, C. A. Bouman, G. T. Buzzard, and B. Wohlberg, "Plug-and-play methods for integrating physical and learned models in computational imaging: Theory, algorithms, and applications," *IEEE Signal Processing Magazine*, vol. 40, no. 1, p. 85–97, Jan. 2023. [Online]. Available: http://dx.doi.org/10.1109/MSP.2022.3199595

[6] K. Zhang, Y. Li, W. Zuo, L. Zhang, L. V. Gool, and R. Timofte, "Plug-and-play image restoration with deep denoiser prior," 2021.

[7] K. Zhang, W. Zuo, and L. Zhang, "Ffdnet: Toward a fast and flexible solution for cnn-based image denoising," *IEEE Transactions on Image Processing*, vol. 27, no. 9, p. 4608–4622, Sep. 2018. [Online]. Available: http://dx.doi.org/10.1109/TIP.2018.2839891

[8] M. Tassano, J. Delon, and T. Veit, "An Analysis and Implementation of the FFDNet Image Denoising Method," *Image Processing On Line*, vol. 9, pp. 1–25, 2019, https://doi.org/10.5201/ipol.2019.231.

[9] S. V. Venkatakrishnan, C. A. Bouman, and B. Wohlberg, "Plug-and-play priors for model based reconstruction," in *2013 IEEE Global Conference on Signal and Information Processing*, 2013, pp. 945–948.

[10] U. S. Kamilov, H. Mansour, and B. Wohlberg, "A plug-and-play priors approach for solving nonlinear imaging inverse problems," *IEEE Signal Processing Letters*, vol. 24, no. 12, pp. 1872–1876, 2017.